Astron. Astrophys. 321, 935–944 (1997)

ASTRONOMY
AND
ASTROPHYSICS

Nonlinear wave heating of solar coronal loops

S. Poedts and J.P. Goedbloed

FOM-Institute for Plasma Physics 'Rijnhuizen', P.O.Box 1207, 3430 BE Nieuwegein, The Netherlands

Received 23 September 1996 / Accepted 15 November 1996

Abstract. The heating of magnetically closed structures (loops) in the solar corona by the resonant absorption of incident waves is studied by means of numerical simulations in the framework of nonlinear resistive magnetohydrodynamics (MHD). It is shown that the dynamics in the resonant layer is indeed very nonlinear for typical coronal parameters. The effect of the nonlinearity on the efficiency of the resonant heating mechanism is investigated. It turns out that this heating mechanism may be less efficient than concluded from the linear MHD studies. As a matter of fact, the modification of the background magnetic field results in a shift of the resonance positions in time which in turn yields broader dissipation layers.

Key words: Sun: corona; magnetic fields; oscillations – MHD

1. Introduction

In spite of numerous theoretical investigations and observational campaigns no conclusive explanation has been found for the long-standing problem of the heating of the solar corona. There is a general consensus that the magnetic field plays a dominant role in this problem and heating by dissipation of magnetic waves, Alfvén waves in particular, is one of the strong proponents. The basic idea of the wave heating mechanism is still the same as in the late forties (Biermann 1946; Schwarzschild 1948) enriched with a leading role of the magnetic field: *magnetic waves* which are generated by the (overshooting) turbulent convective motions in the photosphere transport the required energy through the chromosphere to the corona, guided by the *magnetic field*; in the corona these waves then dissipate their energy in the *magnetic coronal loops*. In this paper, we concentrate on the most difficult part of the whole scenario: the dissipation of the wave energy in the magnetic loops.

The popularity of Alfvén wave heating is based on *observational evidence*, e.g. from the non-thermal broadening of transition and coronal spectrum lines (Zirker 1993) which is ascribed to Alfvén waves (Doschek et al. 1976; Cheng et al. 1979; O'Shea et al. 1996), and on *theoretical investigations* which showed that Alfvén waves can be dissipated efficiently under coronal conditions (Hollweg 1991; Poedts et al. 1989a, 1989b, 1990a, 1990b). However, most theoretical studies of Alfvén wave heating are done in the framework of linearized MHD. In other words, usually it is assumed that the waves are nothing but small-amplitudes perturbations of a fixed background. This assumption may yield a good approximation in the bulk part of a coronal loop but it is challenged in the resonance layers themselves where the fields develop a nearly-singular behaviour, due to the very high magnetic Reynolds numbers in the hot coronal plasma. The high wave amplitudes in the resonant layers may induce nonlinear effects which may yield a different picture of the wave heating mechanism. The *objectives* of the present paper are

1. to show that the dynamics of the resonant layer is indeed very nonlinear, even for very small amplitudes of the incident waves;
2. to show that the resonant dissipation mechanism may be less efficient than concluded from linear theory due to nonlinear mode coupling and the variation of the background fields in time.

The *resonant* dissipation of the wave energy is simulated numerically. We here consider side-ways excitation as opposed to footpoint excitation, which has been studied in a previous paper (Poedts & Boynton 1996). In the next section, the physical model, i.e. the cylindrical coronal loop model and the nonlinear MHD equations, used for the present investigations is given and motivated. In order to appreciate the results of numerical simulations, some information on the applied discretisation techniques is required. This information is given in Sect. 3. The results of the numerical simulations of the time-dependent nonlinear MHD behaviour of an externally driven cylindrical coronal loop model are given in Sect. 4. In Sect. 5, the consequences of these nonlinear simulations for solar coronal loop heating are discussed.

2. Physical model

2.1. Configuration

Magnetic loops can be considered as the 'building blocks' of the solar corona (Priest 1990). They can be up to 700.000 km long

Send offprint requests to: S. Poedts

and have radii that vary from 1.000 km to 10.000 km, where the longer loops have larger radii (Priest 1984). The aspect ratio $A \equiv L/2\pi a$, with L the length of the loop and a the small radius, is typically 8 (Beaufumé et al. 1992). Hence, the cylindrical plasma column considered in the present paper yields a good approximation for the coronal loops. Nothing much is known about the internal structure of these magnetic loops, which makes it difficult to obtain conclusive simulation results on their heating. For resonant absorption, for instance, the radial structure of the loops is very important for the efficiency and the localisation of the heat deposition in the loops (see e.g. Poedts et al. 1989a, 1989b, 1990a, 1990b). Hence, by lack of observational data, in the next subsection we consider a simple but reasonable coronal loop model.

We consider a straight cylindrical plasma column of length L and radius a. The plasma column is side-ways driven by waves which are incident on it. The initial state considered in the present simulations is given in Sect. 4. The external medium is not included in the model. As a matter of fact, the excitation of the coronal loop by an incident wave is numerically simulated by specifying the amplitude and wavenumbers at the surface of the loop (see Sect. 5). The anchoring of the magnetic field lines in the dense photosphere is *not* taken into account in the present study but its effect will we discussed in a forthcoming paper.

2.2. Nonlinear MHD equations

The results presented in Sect. 4 are based on numerical solution of the resistive MHD equations. The single fluid model is used. In dimensionless form, these equations can be written as:

$$\rho \frac{\partial \boldsymbol{V}}{\partial t} = -\boldsymbol{V}\cdot\nabla\boldsymbol{V} - \nabla p + (\nabla\times\boldsymbol{B})\times\boldsymbol{B}, \quad (1)$$

$$\frac{\partial \boldsymbol{B}}{\partial t} = \nabla\times(\boldsymbol{V}\times\boldsymbol{B}) - \nabla\times(\eta\nabla\times\boldsymbol{B}), \quad (2)$$

$$\frac{\partial p}{\partial t} = -\nabla\cdot(p\boldsymbol{V}) - (\gamma-1)p\,\nabla\cdot\boldsymbol{V} + (\gamma-1)\eta(\nabla\times\boldsymbol{B})^2, \quad (3)$$

$$\frac{\partial \rho}{\partial t} = -\nabla\cdot(\rho\boldsymbol{V}), \quad (4)$$

$$\nabla\cdot\boldsymbol{B} = 0. \quad (5)$$

Here, ρ, p, $\boldsymbol{V}$, and $\boldsymbol{B}$ denote the plasma density, the plasma pressure, the velocity field, the magnetic field, and the gravitational accelleration, respectively. The ratio of specific heats, γ, is assumed to be 5/3. The magnetic permeability, μ, has been set equal to one. The divergence equation, $\nabla\cdot\boldsymbol{B} = 0$, serves as an initial condition on $\boldsymbol{B}$. In the dimensionless set of Eqs. (1)–(5), lengths are normalized to the characteristic scale of the cylindrical system, i.e. to the plasma radius (a), and magnetic fields, velocities, and times are normalized to the initial longitudinal magnetic field on axis (B_0), the Alfvén velocity ($V_A = B_0/\sqrt{\rho}$), and the Alfvén crossing time ($\tau_A = a/V_A$), respectively.

2.3. Approximations

Gravity has been ignored in the equations above. Gravity breaks down the axial symmetry and induces a stratification of the density along the loop and, hence, linear mode coupling in this direction (see e.g. Poedts & Goossens 1991; Beliën et al. 1996). In the present paper, we want to study nonlinear mode coupling and its effects on resonant absorption.

The continuity equation (4), which describes the evolution of the plasma density ρ, is not included in the present formulation. The plasma density is assumed to be constant in space and time, i.e. $\rho \equiv 1$. Electric resistivity η is the only dissipative effect considered. The electric resistivity is defined as a scalar quantity with a dependence on the plasma radius only and not on the time. In the present paper, the (dimensionless) plasma resistivity is defined as

$$\eta \equiv \eta_* \frac{J_{0z}(r_*)}{J_{0z}(r)}, \quad (6)$$

with η_* a constant and $J_{0z} \equiv J_z(t = 0)$ the longitudinal current density in the initial state (see Sect. 2.4). The constant η_* denotes the resistivity at the position r_* which will be specified below as the ideal resonance position. The magnetic Reynolds number at the center R_0 is $1/\eta(0)$.

2.4. Initial state

All simulations discussed in Sect. 4 start from the same initial state: a static, axisymmetric cylinder with a constant density, a constant z-component of the magnetic field, and a parabolic current density profile in the longitudinal direction. In dimensionless units, we have:

$$\rho_0 \equiv \rho(t = 0) = 1, \quad (7)$$

$$B_{0z} \equiv B_z(t = 0) = 1, \quad (8)$$

$$J_{0z} \equiv J_z(t = 0) = j_0\,(1 - r^2), \quad (9)$$

and, hence,

$$B_{0\theta} \equiv B_\theta(t = 0) = 0.25\,j_0\,r(2 - r^2), \quad (10)$$

and

$$P_0 \equiv P(t = 0) = \frac{j_0^2}{48}\,(1 - r^2)^2(5 - 2r^2). \quad (11)$$

The safety factor $q \equiv rB_{0z}/AB_{0\theta}$, which measures the pitch of the magnetic field, is 1 on axis ($r = 0$) and 2 at the plasma surface ($r = 1$) for the typical choice of parameters made here, viz. $j_0 = 0.2$ and $A = 10$.

3. Three-dimensional nonlinear simulations

In this section, the problems of the strongly localized plasma dynamics and of the widely disparate MHD time scales and the numerical methods applied to overcome these numerical problems are addressed briefly. More details on these numerical techniques are given in Appendix A.

3.1. Strongly localized solutions

The linearized ideal MHD equations contain mobile singularities which give rise to continuous parts in the MHD spectrum of oscillation frequencies of a coronal loop. When such a coronal loop is excited side-ways at a frequency within the range of the continuous spectrum, ideal resonances occur inside the plasma at the flux surfaces where the local Alfvén frequency matches the frequency of the external driver, i.e. the incident wave. The non-zero plasma resistivity removes the singularity from the MHD equations but for the relevant, very small, values of η in the solar corona, the resonant behaviour is clearly present. As a result, the plasma solutions become very localized in the radial direction. To simulate such behaviour accurately on a computer requires local expansion functions in this direction. In our code, we used *finite differences* on two *staggered meshes* in the radial direction and a *spectral discretization* (Fourier modes) in the θ- and z-direction in which such strong localizations do not occur.

3.2. Widely disparate time scales

Widely disparate time scales are another problem when simulating the three-dimensional nonlinear dynamical behaviour of an elongated coronal loop on a computer. The ideal MHD spectrum consists of three subspectra: the fast magnetosonic subspectrum and the Alfvén and slow magnetosonic subspectra with the mentioned continuous parts. In cylindrical geometry, the time scale associated with the compressional fast magnetosonic wave, also called the compressional time scale, is measured by the transit time of the fast magnetosonic wave over the plasma radius a, $\tau_{\rm Fast} \equiv a/V_F$, with V_F the phase velocity of the fast magnetosonic wave. For the low β plasmas in solar coronal loops, $V_F \approx V_A$ and, hence, $\tau_{\rm Fast} \approx a/V_A$ (β is the ratio of the plasma pressure and the magnetic pressure, $\beta \equiv 2\mu P/B^2$). Shear Alfvén waves, on the other hand, propagate mainly along the magnetic field lines and, hence, the time scale related to these waves is measured by the transit time of the shear Alfvén wave over the *length* of the coronal loop L: $\tau_{\rm Alfven} \equiv L/V_A$. In the large aspect ratio loops that are observed in the corona of the sun, the time scales $\tau_{\rm Fast}$ and $\tau_{\rm Alfven}$ differ substantially. As a matter of fact, in the cylindrical model that is used in the present paper, the fast magnetosonic time scale is much shorter than the shear Alfvén time scale: $\tau_{\rm Alfven}/\tau_{\rm Fast} = L/a = 2\pi A = 20\pi$ for $A = 10$.

When the heating of coronal loops is studied, the time scale of resistive diffusion of magnetic fields, $\tau_{\rm Diff} \equiv \mu_0 a^2/\eta$, is also of interest. In coronal plasmas, where the magnetic Reynolds number $R_m = \tau_{\rm Fast}/\tau_{\rm Diff}$ is typically $10^{10} - 10^{12}$, the diffusion time scale of the background field is much longer that both $\tau_{\rm Fast}$ and $\tau_{\rm Alfven}$. In the resonant absorption mechanism, however, plasma heating takes place on a shorter time scale than $\tau_{\rm Diff}$ as a result of the short length scales created by the resonances. The width of the resonant layer scales as $\eta^{1/3}$ and, hence, the time scale of resonant absorption $\tau_{\rm RA} \sim \eta^{-1/3}$. Clearly, $\tau_{\rm RA}$ is also longer than the Alfvén time scale. Hence, in the elongated coronal loops we have

$$\tau_{\rm Fast} \ll \tau_{\rm Alfven} < \tau_{\rm RA} \ll \tau_{\rm Diff}. \tag{12}$$

The fast magnetosonic waves play the important role of 'energy-carrier': They are responsible for the transport of the energy from the source, across the magnetic surfaces, to the resonant layer(s).

3.3. Numerical scheme

The widely disparate time scales (12) make three-dimensional nonlinear time dependent MHD calculations very expensive because of the time-step limitation for conventional explicit numerical schemes. This limitation follows from the Courant-Friedrichs-Lewy (CFL) stability condition imposed by the compressional fast magnetosonic motion. Indeed, explicit numerical schemes are stable only if the time step Δt is smaller than $\Delta r/V_A$ or

$$\Delta t \leq \frac{\Delta r}{a}\,\tau_{\rm Fast} \ll 1, \tag{13}$$

where Δr is the smallest mesh interval in the radial direction. The high radial resolution ($\Delta r \ll a$) required to resolve the resonant layers that occur and the small fast magnetosonic time scale ($\tau_{\rm Fast} \ll \tau_{\rm Alfven} \equiv 1$) make this CFL condition extremely restrictive for numerical simulations of coronal loop heating which occurs on a much longer time scale (see Eq. (12)).

The results presented in the next section are obtained by means of a semi-implicit predictor-corrector scheme. In this method, the CFL restriction on the fast magnetosonic waves is avoided by treating these waves, and only these, implicitely. Some more details on the spatial discretization and on the semi-implicit algorithm we used can be found in Appendix A. This method was applied to the numerical simulation of time dependent MHD phenomena for the first time by Harned & Kerner (1985). Since then, it has been used by many authors to simulate the MHD behaviour of both laboratory plasmas (tokamaks, stellerators, etc.) and solar plasmas (see e.g. Harned & Kerner 1986; Harned & Schnack 1986; Schnack et al. 1987; Lerbinger & Luciani 1991, etc.).

4. Results

The numerical code described above has been applied to study the heating of a solar coronal loop by the resonant absorption of an incident wave with a given amplitude and given wave numbers m and n (see Sect. 5). The results are presented in this section. In Sect. 4.1, the main linear MHD results on time scales and localisation of the heating are reproduced as a check and brief reminder. In Sect. 4.2, the variation of the background magnetic field is demonstrated. Next, nonlinear mode coupling is shown to occur in the resonant layer in Sect. 4.3. Finally, in Sect. 4.4 the implications of this nonlinear mode coupling for the resonant aborption heating mechanism are discussed.

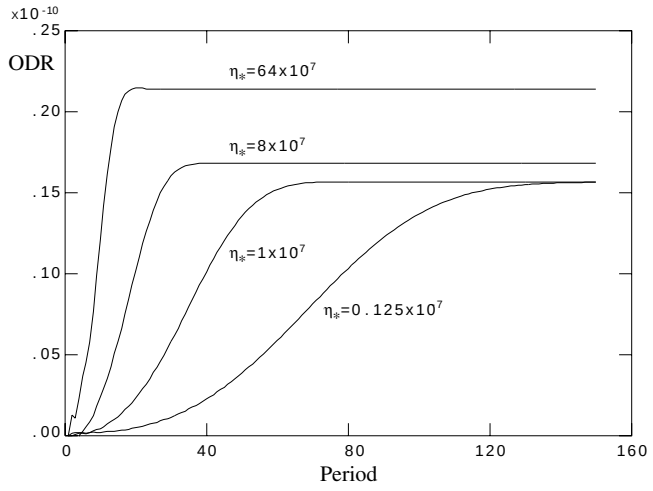

Fig. 1. Average Ohmic dissipation rate versus number of driving periods for different values of the plasma resistivity: a) $\eta_* = 64 \times 10^{-7}$, b) $\eta_* = 8 \times 10^{-7}$, c) $\eta_* = 1 \times 10^{-7}$, d) $\eta_* = 0.125 \times 10^{-7}$.

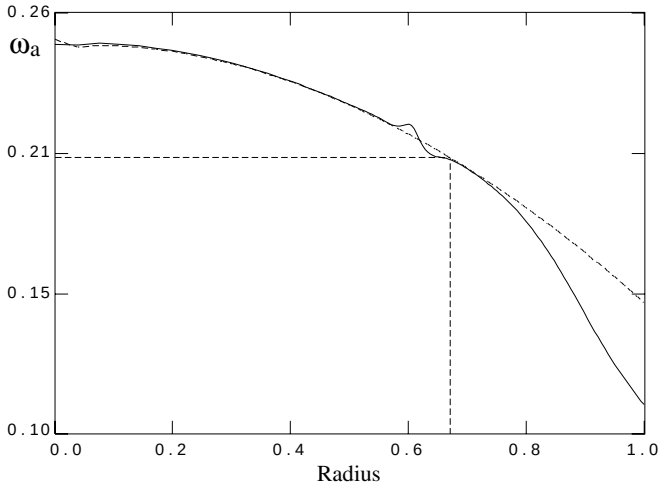

Fig. 2. Radial profile of the local Alfvén frequency at $t = 0$ (dotted line) and the average over the 80th driving period (full line). The linear resonance position is also indicated, i.e. $\omega_d = 0.205 = \omega_A(0.671)$.

4.1. Main linear MHD results

The main linear MHD results on resonant absorption were reconstructed as part of the testing phase of the semi-implicit predictor-corrector scheme. For these simulations only one mode has been updated in each time step (as there is no nonlinear mode coupling in the circular cross-section cylindrical coronal loop model considered here) and the background has been fixed, i.e., the $(m, n) = (0, 0)$-'mode' is not updated but kept constant as specified in Eqs. (1)–(5).

The main linear MHD results were confirmed. When the system is driven at a frequency in the range of the ideal MHD Alfvén continuum, as time evolves the plasma response localizes in an ever diminishing layer around the resonance point, i.e. the point where the local Alfvén frequency matches the frequency of the external driver. Due to the finite electric conductivity ($\eta \neq 0$) this localization stops after a finite time and the system attains a stationary state in which all quantities oscillate harmonically with constant amplitude. This happens when the energy supplied by the external source is exactly balanced by the Ohmic dissipation in the resonant layer. The width of the resonance layer(s) scales as $\eta^{1/3}$, as was already known from linear MHD calculations (see e.g. Kappraff & Tataronis 1977; Poedts et al. 1989a, 1989b). Also, the time scale to reach the stationary state is proportional to $\eta^{-1/3}$, in linear MHD. This can be seen in Fig. 1 where the Ohmic dissipation rate is plotted versus time for different values of the plasma resistivity. It is clear that the Ohmic dissipation rate is small in the beginning of the simulation when all profiles are still smooth and the Ohmic terms do not play a role in the MHD equations. After some time, however, the phase-mixing process has created strong gradients and the resistive terms then become important. As a result, the Ohmic dissipation rate starts to grow. When the stationary state is reached, this grow stops again and the Ohmic dissipation rate is constant in time. The initial time interval in which the Ohmic dissipation rate increases depends clearly on the resistivity. But Fig. 1 also demonstrates a remarkable feature of resonant absorption, viz. that the Ohmic dissipation rate becomes independent of plasma resistivity in the limit $\eta \to 0$. Indeed, in Fig. 1 it can be seen that it takes longer to reach the stationary state for $\eta_* = 0.125 \times 10^{-7}$ than for $\eta_* = 1 \times 10^{-7}$ but the Ohmic dissipation rate is almost exactly the same for both cases. Hence, the main linear results on resonant absorption are confirmed by these test runs for the nonlinear code.

4.2. Variation of the 'background' field

One of the advantages of the used spectral discretization is that the 'background' can be separated from the rest of the plasma response by virtue of the fact that it is given by the $(m, n) = (0, 0)$ 'mode'. In linear MHD simulations of coronal loop heating by the absorption of incident waves, the plasma response to the external driving is assumed to consist of a small perturbation of a *fixed*, usually static, 'background equilibrium'. In nonlinear MHD simulations, the 'background equilibrium' varies in two ways, for two different reasons, and on two different time scales and length scales. First, as mentioned above, the dissipation of the background magnetic field generates flow (and heating!). However, this change of the 'equilibrium' takes place on a long length scale and on a long time scale, viz. the resistive diffusion time scale $\sim R_m$. Second, the build-up and heating of the resonant layer changes the background equilibrium locally. This variation of the background takes place on a shorter time scale, viz. the time scale of resonant absorption, which is proportional to $R_m^{1/3}$. The plasma reacts to the heating process by *trying to stop it* or, at least, to reduce its rate. The most effective way to accomplish this is to modify the background magnetic field and, hence, the profile of the local Alfvén frequency such that the resonance becomes wider.

In the simulations we did, both changes of the background can be observed. In Fig. 2 this is illustrated by plotting the average profile of the local Alfvén frequency over one driving period, together with the initial $\omega_A(r)$-profile ($\omega_A \equiv \boldsymbol{k}\cdot\boldsymbol{B}_0/\sqrt{\rho_0}$). The average is made for driving period number 140, i.e. after a long time so that the effect of the global diffusion of the background magnetic field on the local Alfvén frequency is also visible. Since the plasma resistivity is the largest in the outer layers of the coronal loop, this effect is the largest there. In addition to this global variation, the local heating in the resonant layer around $r = 0.67$ also affects the local Alfvén frequency there. In the resonant layer, the $\omega_A(r)$-profile oscillates around the plotted average building up a 'plateau' at the driving frequency $\omega_d = 0.205$. As a result, the resonant layer widens and, hence, the gradients diminish and the heating process becomes less effective. Clearly, this reduction of the effectiveness of the heating process only works in this case of monoperiodic driving and can not work when the loop is driven by a continuous spectrum of incident waves as would be the case on the sun.

The generated 'background flow' is dominantly in the tangential directions (θ and z) and is the largest in the resonant layer and near the plasma edge.

4.3. Nonlinear mode coupling

Due to the spectral discretization in the tangential directions, the nonlinearity of the dynamics is translated into a coupling of the Fourier modes taken into account. The coupling of the Fourier modes is not to be confused with linear mode coupling which occurs as a result of e.g. geometrical effects or variation of equilibrium quantities in the direction that is discretised by means of Fourier modes or line-tying effects. Such linear mode coupling does not occur in the present simulations where a straight axisymmetric cylinder is considered with a circular cross-section and effects of line-tying have not been considered. Hence, the observed coupling of the Fourier modes is a pure nonlinear effect. This nonlinear mode coupling occurs mainly in the resonant layer because the amplitudes of the fields are the largest there. In the present section, we want to show that the nonlinear mode coupling is *i*) selective, *ii*) restricted to the resonant layer(s), and *iii*) dependent on the amplitude of the incident waves and the plasma resistivity.

4.3.1. Selective mode coupling

In contrast to the linear mode coupling which is the strongest between 'nearest neighbours', the nonlinear mode coupling is more *selective*. Consider a wave with a given frequency and with given wave numbers $m = 2$ and $n = 1$. When this wave is incident on a coronal loop it excites mainly the mode of oscillation charaterized by the same mode numbers. However, in addition, other modes of plasma oscillation are excited by this incident wave. One way to measure the strength of this nonlinear mode coupling is to calculate the amount of kinetic and magnetic energy in each of the modes at a specific point in time. Our simulations show that, as expected, the 'overtones' of the

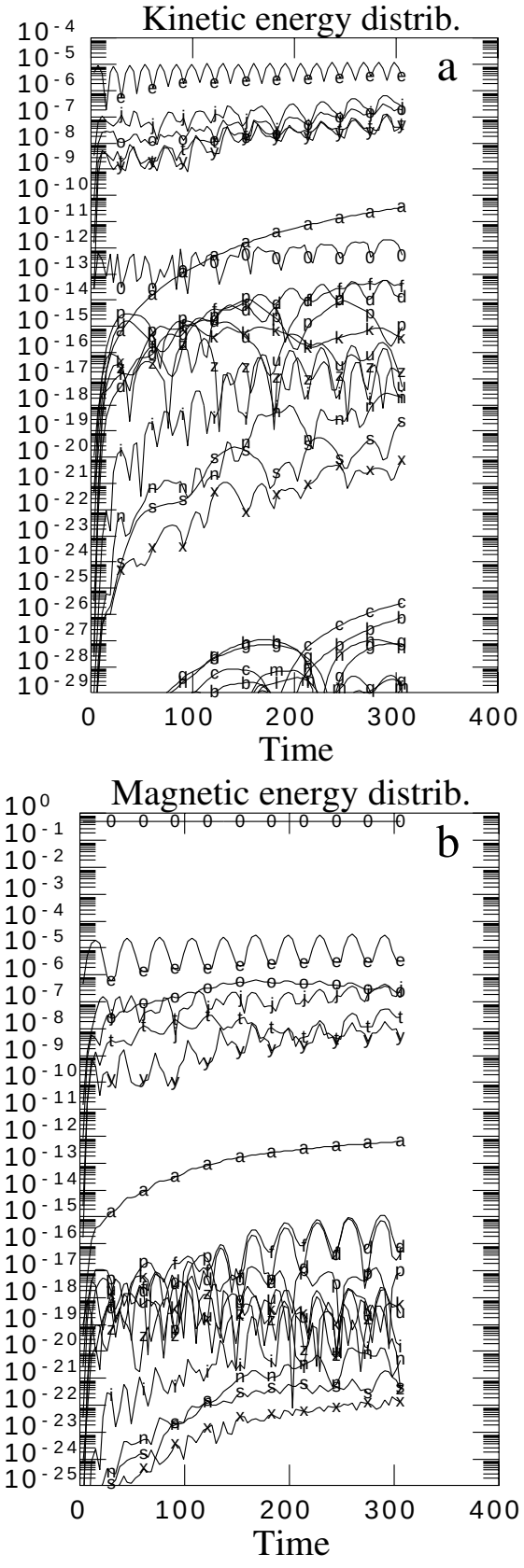

Fig. 3a and b. Modal kinetic (**a**) and magnetic (**b**) energy distribution versus time for $A = 0.003\,V_A$ and $\eta_* = 10^{-5}$. The labels correspond to the mode numbers as displayed in Eq. 14.

basic $(m, n) = (2, 1)$ mode are excited most effectively. In other words, modes with the same helicity as the basic mode, i.e. with the same m/n-ratio, absorb most of the energy of the incident wave. The energy absorbed by the other nearby modes, with a different helicity, is several orders of magnitude lower than the energy absorbed by the overtones. The reason for this is the fact that the excited Alfvén waves are incompressible waves which do not involve a density perturbation. Since we do not update the density in the present simulations, the overtones are in fact the only modes that can be excited nonlinearly. Due to numerical 'noise', however, some of the supplied energy couples to the other modes too. This is demonstrated by the following experiment which was done to check the code and measure the numerical 'noise'. Consider a coronal loop with initial equilibrium profiles given by Eqs. (1)–(5) and a resistivity profile given by Eq. (6) with $\eta_* = 1 \times 10^{-5}$ and excited by an incident wave with wave numbers $(m, n) = (2, 1)$ and amplitude $0.005 \times V_A(0)$ at the loop surface. In the simulation of the plasma response to this excitation the following Fourier modes are taken into account:

$m\backslash n$	0	1	2	3	4	5	6	7	8
10	–	–	–	–	x	**y**	z	–	–
9	–	–	–	–	v	w	–	–	–
8	–	–	–	s	**t**	u	–	–	–
7	–	–	–	q	r	–	–	–	–
6	–	–	n	**o**	p	–	–	–	–
5	–	–	l	m	–	–	–	–	–
4	–	i	**j**	k	–	–	–	–	–
3	–	g	h	–	–	–	–	–	–
2	d	**e**	f	–	–	–	–	–	–
1	b	c	–	–	–	–	–	–	–
0	**0**	a	–	–	–	–	–	–	–

(14)

plus, of course, the Fourier modes with the corresponding mode numbers of opposite sign (the characters refer to the labels in Fig. 3. The modes indicated with bold characters should absorb all the energy, viz. the 'basic' $(m, n) = (2, 1)$ mode, which is the one that is excited directly, the $(0, 0)$ 'background', and the 'overtones' with the same ratio $m/n = 2$ as the basic mode. In order to check the numerical accuracy, a few modes with different helicity are considered as well. The amount of energy contained in these modes should remain zero. In Fig. 3 the kinetic (a) and magnetic (b) energy distribution are shown versus time. Of course, values below 10^{-16} have no physical meaning (but the standard plotting routine used here plots them anyway).

Clearly, most of the kinetic energy is absorbed by the $(2, 1)$ ('e'-) mode which is the driven mode. During the time interval considered in the present simulation, which comprises 20 driving periods, i.e. $20 \times 2\pi/\omega_d$, the overtones $(4, 2)$, $(6, 3)$, $(8, 4)$, and $(10, 5)$ ('j', 'o', 't', and 'y', respectively) absorb roughly about 1-10% (each) of the energy absorbed by the 'basic' mode. The kinetic energy contained in the other modes, with a different helicity, however, remains at least eight orders of magnitude lower than the kinetic energy of the basic mode, which means that the accuracy of the calculation is all right. Notice that the background $((0, 0))$ also absorbs some kinetic energy related

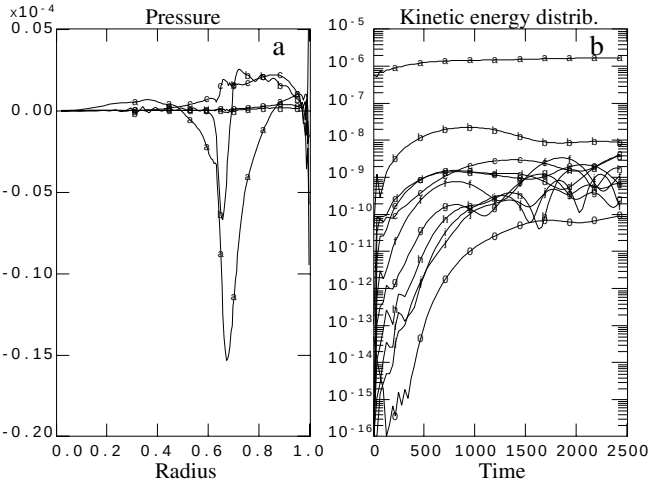

Fig. 4. a Modal contributions to the radial pressure profile and **b** modal kinetic energy distribution versus time for $A = 0.001\, V_A$, $\eta_* = 8 \times 10^{-7}$, and $t = 80\, P_d$.

to the flow generated in the equilibrium, as mentioned above. The magnetic energy of the background of course dominates the magnetic energy contained in the incident wave which, again, is only contained in the basic $(2, 1)$ mode and in its overtones. However, although these modes absorb only little energy they might play an important role in the heating process because the small-scale modes might affect the effective viscosity and resistivity felt by the large-scale modes. But it is extremely expensive (CPU time and computer memory) to take all these modes along in a three-dimensional simulation. Therefore, in the remainder of this paper, the simulations are done with only the *overtones* of the basic mode and the effect of the small-scale modes on the effective viscosity and resistivity is not investigated here.

4.3.2. Small plasma resistivity

The strength of the mode coupling discussed above is a measure for the nonlinearity of the dynamics. The mode coupling is restricted to the resonant layer that builds up around the idealy singular plasma layer. This is illustrated in Fig. 4a where the contribution of the different Fourier modes to the plasma pressure is plotted versus the loop radius. Outside the resonant layer around $r = 0.671$ the amplitudes of the overtones are almost zero, indicating that the dynamics is linear there. But inside the resonant layer the amplitudes of the overtones become comparable to the amplitude of the basic mode and the overtones contribute substantially to the dynamics of this resonant layer, which is therefore nonlinear. The nonlinearity of the dynamics of the resonant layer depends on the magnetic Reynolds number. This is illustrated by comparing Fig. 4 to Fig. 6 which is the result of exactly the same simulation but with an eight times larger magnetic Reynolds number. From Fig. 6 it is clear that the dynamics in the resonant layer can become very nonlinear, even for relatively small values of the amplitudes of the incident waves, which makes realistic coronal loop heating simulations

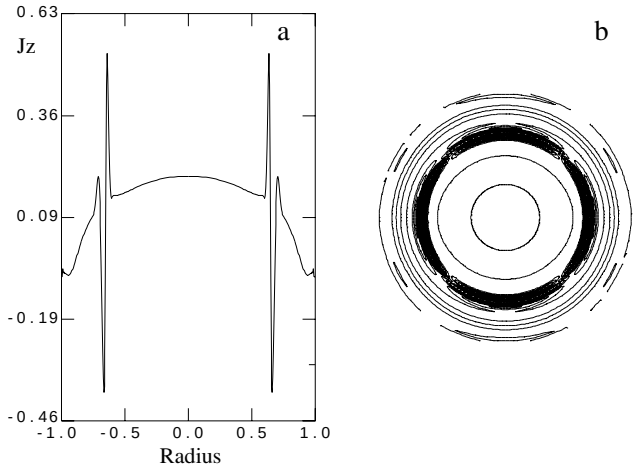

Fig. 5. a Radial profile and **b** contour lines on a poloidal cross-section of the longitudinal current density for $A = 0.001\,V_A$, $\eta_* = 8 \times 10^{-7}$, and $t = 80\,P_d$.

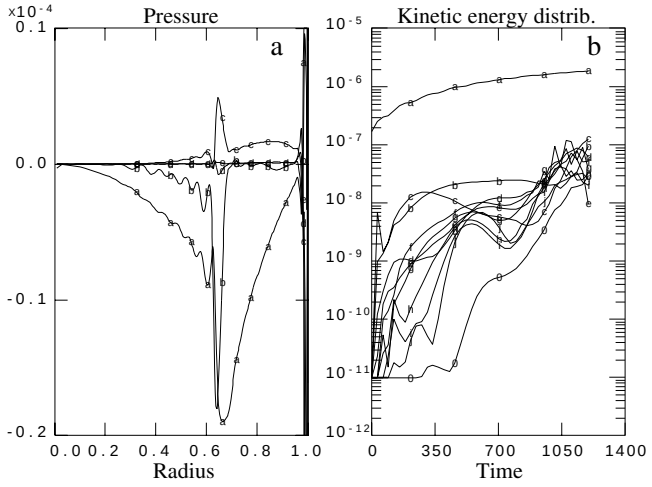

Fig. 6. a Modal contributions to the radial pressure profile and **b** modal kinetic energy distribution versus time for $A = 0.001\,V_A$, $\eta_* = 10^{-7}$, and $t = 40\,P_d$.

very expensive. As a matter of fact, for the very small η-values of interest ($\eta < 10^{-10}$), the narrow resonance layers require very small grid spacing and, hence, very small time steps and, in addition, many modes have to be taken into account in order to resolve the nonlinear mode coupling.

Fig. 5 displays a snapshot of the longitudinal component of the current density after 80 driving periods. The initial parabolic current density profile is still clearly visible in this case but the perturbation is nonlinear. In fact, after 80 driving periods, the perturbation on the current density is already very localized and the amplitude in the resonant layer is more than two times larger than the initial current density there, in spite of the relatively low driving amplitude at $r = 1$, viz. $0.001\,V_A$.

For smaller values of η_*, the current density is even more localized, as shown Fig. 7 where a snapshot of the current density

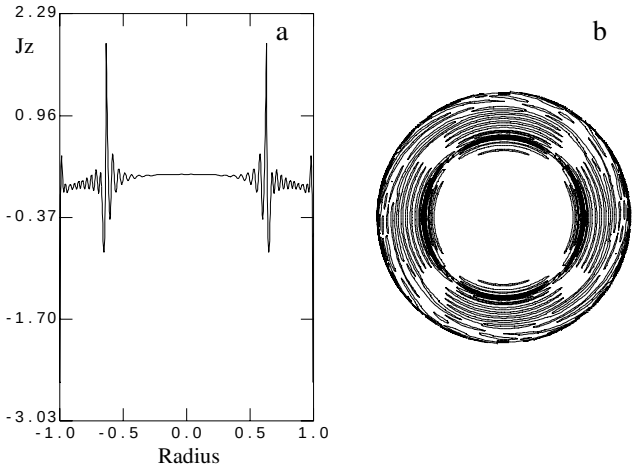

Fig. 7. a Radial profile and **b** contour lines on a poloidal cross-section of the longitudinal current density for $A = 0.001\,V_A$, $\eta_* = 10^{-7}$, and $t = 40\,P_d$.

is displayed for $\eta_* = 10^{-7}$ after 40 driving periods and for the same driving amplitude as in Fig. 5. The snapshot is taken earlier (after 40 P_d) and the phase-mixing process is not finished yet, which explains the many narrow current layers observed in this snapshot.

4.3.3. Large amplitude waves

Clearly, the amplitude of the plasma response is also determined by the amplitude of the incident waves. The waves observed in the solar corona have amplitudes of up to 40 km/s (Hollweg & Yang 1988), i.e. 1 to 2% of the typical coronal value of the Alfvén velocity (2000 km/s). In the previous sections we have seen that driving amplitudes of the order of 0.1% of the background Alfvén velocity already yield very nonlinear behaviour in the resonant layers, due to the extremely low plasma resistivity in the hot coronal loops.

Fig. 8 displays a snapshot of the longitudinal current density for a driving amplitude of 0.3% of the background Alfvén velocity and a relatively high plasma resistivity, viz. $\eta_* = 10^{-5}$. It is clear that the nonlinear effects are very dominant in this case and the resonant layer does not stay nicely at the same radial position anymore. The variation of the background and the nonlinear mode coupling are very substantial in this case. As a matter of fact, the modal kinetic energy distribution shows that the amount of energy in the 'overtones' becomes comparable to the amount of energy in the excited mode and the plasma behaviour looks very much like MHD turbulence in this large amplitude case. As a result, the heat deposition is spread over the whole loop volume. It is to be noted, however, that this run was performed with a resolution of 128×24 and the 24 modes may be insufficient to resolve the nonlinear mode coupling in this case. The above discussion on the heat deposition brings us to the important issue of the effects of the nonlinearity in the resonant layers on the efficiency of the heating mechanism and the

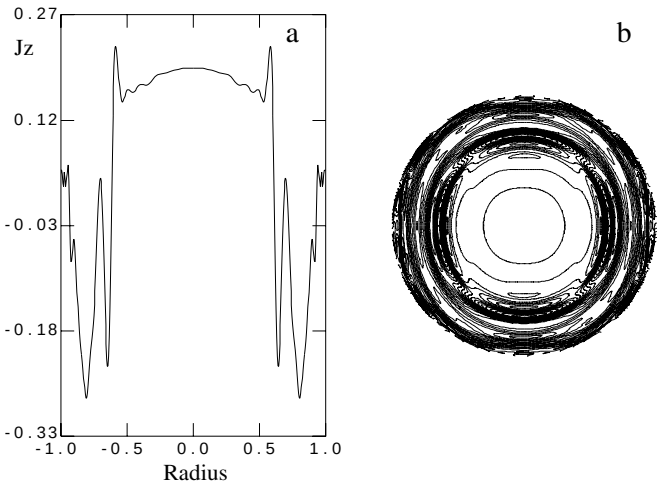

Fig. 8. a Radial profile and **b** contour lines on a poloidal cross-section of the longitudinal current density for $A = 0.003\,V_A$, $\eta_* = 10^{-5}$, and $t = 20\,P_d$.

localization of the heat deposition. These points are discussed in the next section.

4.4. Effects on resonant absorption

In Sect. 4.2 we have seen that the 'background', i.e. the $(m, n) = (0, 0)$-mode, changes in two different ways, on two different time scales. First, there is a global change of the background magnetic field due to the magnetic diffusion. This is a slow change on a time scale $\sim \eta^{-1}$. Due to the choice of the η-profile (6), the magnetic diffusion is much faster near the loop boundary than in the loop center. The second change of the background is much more local and due to the resonant dissipation of the supplied wave energy. It occurs on a much shorter time-scale $\sim \eta^{-1/3}$ and the variation of the background magnetic field is localized in a relatively thin layer around the ideal resonance position. The changes of the background magnetic field influence both the efficiency of the heating process and the localization of the heat deposition. As a matter of fact, any change of the local Alfvén frequency changes the resonance positions and, hence, the locations where the heat is deposited. Moreover, the linear MHD studies have shown that the efficiency of the heating process depends on the gradients of the background fields. The time scale for resonant heating, e.g., scales with $(\partial\omega_A/\partial r)^{-2/3}$. The average effect of the background variation, as discussed in Sect. 4.2, therefore leads to *less efficient* heating as compared to linear MHD simulations.

On the other hand, the variation in time of the local Alfvén frequency results in a continuous shifting of the resonance position(s) when the external driving frequency is kept constant. As a result, the heat deposition profile changes in time and, for very nonlinear cases, this means that the heat deposition is spread over the whole loop volume instead of in a narrow resonant layer, as would be concluded from linear MHD simulations. For weakly nonlinear cases too, the 'flattening' of the local Alfvén frequency profile near the resonance layer leads to wider resonance layers and less localized heat deposition profiles.

5. Discussion and conclusions

The resonant dissipation of Alfvén waves in coronal loops is a promising explanation for the high temperatures in the solar corona. We have studied the resonant heating mechanism in the framework of nonlinear resistive MHD and focussed on the dynamics of the resonant layers. The simulations presented in this paper clearly demonstrate that the dynamics of the shear flow in the resonant layers is very nonlinear for typical coronal loop parameter values. The nonlinearity manifests itself by the excitation of 'overtones' of the incident waves. For typical coronal parameter values this nonlinear mode coupling is quite substantial and, hence, nonlinear effects need to be taken into account when deriving quantitative results on the efficiency of resonant absorption as a coronal heating mechanism.

From the numerical simulations discussed here one can conclude that the heating rate due to resonant dissipation is lower than the heating rate predicted by linear MHD simulations, in spite of the fact that the nonlinear mode coupling yields an energy cascade to smaller length scales. This qualitative statement is quantified by Poedts et al. (1996), who calculated the actual Ohmic dissipation rate for a linear MHD simulation that is continued in nonlinear MHD.

It is important to notice that for conclusive statements about the role of wave heating in the solar corona the relatively simple model used in the present paper should be improved by including, e.g., density variation, effects of line-tying, thermal conduction, etc. Also, more and better observations are required of the internal structure of the coronal loops, both in the radial and in the longitudinal direction. The radial structure is most important for heating by resonant absorption because it is the stratification in the radial direction which determines the time scales and the localisation of the heat deposition. Moreover, information is required on the waves that might cause these changes, i.e., on the power spectrum of the waves that excite the coronal loops both side-ways and at the footpoints.

Acknowledgements. The authors wish to thank their colleagues A. Hearn and M. Kuperus for many interesting discussions and suggestions. This work was performed as part of the research programme of FOM with financial support from NWO. This work was sponsored by the Stichting Nationale Computerfaciliteiten (National Computing Facilities Foundation, NCF) for the use of supercomputer facilities, with financial support from NWO.

Appendix A: the numerical method

In this appendix, some details are presented about the numerical code that produced the results shown in the present paper. The semi-implicit predictor-corrector scheme is not new and has been applied to numerical simulations of three-dimensional time-dependent MHD phenomena before. In fact, our code is

based on the code Biskamp & Welter (1987) used to study sawtooth disruptions in tokamaks. Yet, many variations on the semi-implicit algorithm are possible and we modified the scheme used by Biskamp and Welter. In this appendix, only the main features of the algorithm we used are given. More detailed information on the semi-implicit method can be found elsewhere (see e.g. Harned & Kerner 1985; Harned & Kerner 1986; Harned & Schnack 1986; Lerbinger & Luciani 1991).

A.1. Spatial discretisation

In the θ- and the z-direction, the plasma response to the external driving can be expected to be relatively smooth so that global expansion functions can be used to discretize these directions. The physical variables f are expanded in a Fourier series:

$$f(r,\theta,z;t) = \sum_m \sum_n f_{mn}(r;t) e^{i(m\theta + \frac{2\pi}{L} nz)}. \tag{A1}$$

The nonlinear terms in the MHD equations then need careful treatment because these terms are products in real space, which lead to convolution sums in Fourier space. These convolution sums are a CPU time consuming operation which is not vectorizable.

For the spatial discretization of the radial direction, on the other hand, finite differences are used. Due to the occurence of resonances, the solutions can become extremely localized in the radial direction excluding the possibility of using global expansion functions for the spatial discretization in this direction. Two staggered meshes are used. This is necessary to obtain a correct representation of the linear MHD spectrum and to satisfy certain vector identities identically, e.g. $\nabla \cdot \nabla \times \boldsymbol{u} = 0$, in finite different form so that $\nabla \cdot \boldsymbol{B} = 0$ can be implemented as an initial condition on the magnetic field. The quantities V_r, B_r, J_θ, and J_z are defined on the 'integer' mesh $\{r_i \,|\, r_1 = 0 < \ldots < r_i < r_{i+1} < \ldots < 1 = r_{N_r}, i = 2, \ldots, N_r - 1\}$, where N_r is the number of radial mesh points. The quantities V_θ, V_z, B_θ, B_z, J_r and P are defined on the 'half-integer' mesh $\{r_{i+\frac{1}{2}} \,|\, 0 < r_{\frac{1}{2}} < \ldots < r_{i+\frac{1}{2}} < \ldots < r_{N_r-\frac{1}{2}} < 1, i = 0, \ldots, N_r - 1\}$, with $r_{i+\frac{1}{2}} \equiv (r_i + r_{i+1})/2$. Quantities which are defined on the integer (half-integer) mesh are calculated, if needed, on the half-integer (integer) mesh by simple averages, e.g. $B_r(r_{i+\frac{1}{2}}) = (B_r(r_i) + B_r(r_{i+1}))/2$. Two 'virtual' points $r_{-\frac{1}{2}}$ and $r_{N_r+\frac{1}{2}}$ are introduced to calculate such averages at the boundaries $r = 0$ and $r = 1$, respectively. These additional mesh points are defined by

$$0 = \frac{r_{\frac{1}{2}} + r_{-\frac{1}{2}}}{2} \qquad \text{and} \qquad 1 = \frac{r_{N_r-\frac{1}{2}} + r_{N_r+\frac{1}{2}}}{2}. \tag{A2}$$

These two additional mesh points are used to impose regularity conditions in $r = 0$ and boundary conditions in $r = 1$ for the variables which are defined on the half-integer mesh (see section A.3). The two staggered meshes do not need to be uniform. The mesh points can be accumulated whenever this is necessary, e.g. at the resonant layer and/or at the plasma boundary.

A.2. Time advance

The semi-implicit predictor-corrector scheme of Harned & Kerner (1985) is used. This scheme avoids both the overly restrictive CFL condition for the compressional fast magnetosonic waves on the time step in explicit schemes and the complexity and computational intensity of implicit schemes by treating the fast magnetosonic waves, and only these, implicitely in the linear phase. This is accomplished by adding and subtracting, at different time steps, a simple approximation of the term that yields the fast magnetosonic waves in the momentum equation. We use the same 'semi-implicit' term as Harned and Kerner which involves only the velocity components in the $r - \theta$ plane:

$$S(\boldsymbol{V}) \equiv (\Delta t)^2 A_0^2 \nabla_\perp (\nabla \cdot \boldsymbol{V}_\perp), \tag{A3}$$

where A_0 is a constant. Notice that this term does not affect the solution as $\Delta t \to 0$. However, the algorithm we use differs somewhat from the algorithm used by Harned & Kerner (1985) and by Biskamp & Welter (1987): the stabilizing semi-implicit term is applied both in the predictor step and in the corrector step and the Crank-Nicolson-type advance is applied to both $\boldsymbol{V}$ and $\boldsymbol{B}$. The scheme then reads:
predictor step:

$$\begin{aligned}
\boldsymbol{V}^* - \boldsymbol{S}(\boldsymbol{V}^*) &= \boldsymbol{V}^n - \boldsymbol{S}(\boldsymbol{V}^n) + \alpha \Delta t F_V(\boldsymbol{V}^n, \boldsymbol{B}^n, P^n), \\
\boldsymbol{B}^* &= \boldsymbol{B}^n + \alpha \Delta t F_B(\boldsymbol{V}^*, \boldsymbol{B}^n, P^n), \\
P^* &= P^n + \alpha \Delta t F_P(\boldsymbol{V}^*, \boldsymbol{B}^*, P^n),
\end{aligned} \tag{A4}$$

corrector step:

$$\begin{aligned}
\boldsymbol{V}^{n+1} - \boldsymbol{S}(\boldsymbol{V}^{n+1}) &= \boldsymbol{V}^n - \boldsymbol{S}(\boldsymbol{V}^n) + \Delta t F_V(\boldsymbol{V}^*, \boldsymbol{B}^*, P^*), \\
\boldsymbol{B}^{n+1} &= \boldsymbol{B}^n + \Delta t F_B\left(\frac{\boldsymbol{V}^{n+1} + \boldsymbol{V}^n}{2}, \boldsymbol{B}^*, P^*\right), \\
P^{n+1} &= P^n + \Delta t F_P\left(\frac{\boldsymbol{V}^{n+1} + \boldsymbol{V}^n}{2}, \right. \\
&\qquad \left. \frac{\boldsymbol{B}^{n+1} + \boldsymbol{B}^n}{2}, P^n\right),
\end{aligned} \tag{A5}$$

where F_V, F_B, and F_P denote the ideal parts of the right-hand-sides of the MHD Eqs. (1), (2), and (3), respectively. A semi-implicit resistive advance of $\boldsymbol{B}$ and P is performed after the corrector step. Hence, our scheme looks formally much like the scheme used by Lerbinger & Luciani (1991) except for the semi-implicit term itself: Lerbinger and Luciani treat all waves implicitely in the linear phase whereas we used the semi-implicit term of Harned and Kerner which is chosen to make only the fastest time scale implicit in the linear phase and leaving the rest explicit. Lerbinger & Luciani (1991) remarked that the application of the stabilizing semi-implicit term both at the predictor and corrector levels greatly improves the nonlinear stability of the code. If α is chosen to be 0.5, the method is second order accurate in time, with the exception of the fast magnetosonic modes which remain first order accurate due to

Table 1. The boundary conditions at $r = 0$ for different mode numbers.

$m = 0$	$m \neq 0$	$\|m\| = 1$	$\|m\| \neq 1$
$B_z' = 0$	$B_z = 0$	$V_r' = 0$	$V_r = 0$
$V_z' = 0$	$V_z = 0$	$V_\theta' = 0$	$V_\theta = 0$
$P' = 0$	$P = 0$	$B_r' = 0$	$B_r = 0$
		$B_\theta = iB_r$	$B_\theta = 0$

the semi-implicit terms. However, in practice typically $\alpha = 0.51$ or 0.52 is chosen to add some numerical damping in order to reduce numerical noise. The simplicity of the semi-implicit term (A3) with the constant coefficient A_0 avoids the problem of convolutions coupling the individual mode equations. As a result, after discretization, a simple tridiagonal system has to be solved in every predictor and corrector step. This is the only overhead compared to an explicit scheme. Yet, the saving of CPU time accomplished by this simple operation can be very high, up to a factor 1000, due to the fact that the CFL condition on the fast magnetosonic waves is avoided and replaced by the CFL condition imposed by the second-shortest time scale in the problem, viz. the Alfvén time scale (Harned & Kerner 1985).

A.3. Boundary conditions

When the physical variables are expanded in a Fourier series according to Eq. A1, regularity conditions and single-valuedness at the origin $r = 0$ yield analytic conditions for the various m. In particular, the conditions applied at $r = 0$ for $\boldsymbol{V}$, $\boldsymbol{B}$, and P are displayed in Table 1, where the prime denotes the partial derivative with respect to r. At the loop surface $r = 1$, the same boundary conditions are used as for a plasma cylinder surrounded by a perfectly conducting wall, except for the radial component of the velocity field. The incidence of the external wave is numerically simulated by imposing a harmonic oscillation with given frequency and amplitude on the radial velocity component at the loop surface. This yields

$$V_r = (rV_\theta)' = V_z' = B_r = (rB_\theta)' = B_z' = P' = 0 \qquad \text{(A6)}$$

at $r = 1$ for all modes, except for the driven mode, where

$$V_r = A \sin \omega_d t \qquad \text{(A7)}$$

at $r = 1$. Here, A denotes the amplitude of the incident wave and ω_d the driving frequency.

References

Beaufumé, P., Coppi, B., Golub, L. 1992, ApJ, 393, 396

Beliën, A. J. C., Poedts, S., Goedbloed, J. P. 1996, Phys. Rev. Letters, 76, 567

Biermann, L. 1946, Naturwissenschaften, 33, 118

Biskamp, D., Welter, H. 1987, Plasma Physics and Controlled Nuclear Fusion Research, 2, 11

Cheng, C. C., Doschek, G. A., Feldman, U. 1979, ApJ, 227, 1037

Doschek, G. A., Feldman, U., Hoosier, M. E. V., Bartoe, J. D. 1976, ApJS, 31, 417

Harned, D. S., Kerner, W. 1985, J. Comp. Phys., 60, 62

Harned, D. S., Kerner, W. 1986, Nucl. Science and Engineering, 92, 119

Harned, D. S., Schnack, D. D. 1986, J. Comp. Phys., 65, 57

Hollweg, J. V. 1991, in P. Ulmschneider, E. R. Priest, R. Rosner (eds.), Mechanisms of Chromospheric and Coronal Heating, 423, Springer-Verlag, Berlin

Hollweg, J. V., Yang, G. 1988, JGR, 93

Kappraff, J. M., Tataronis, J. A. 1977, J. Plasma Phys., 18, 209

Lerbinger, K., Luciani, J. F. 1991, J. Comp. Phys., 97, 444

O'Shea, E., Doyle, J. G., Erdélyi, R., Dere, K. P., Keenan, F. P. 1996, submitted to AA

Poedts, S., Boynton, G. C. 1996, AA, 306, 610

Poedts, S., Goossens, M. 1991, Solar Physics, 133, 281

Poedts, S., Goossens, M., Kerner, W. 1989a, Solar Physics, 123, 85

Poedts, S., Goossens, M., Kerner, W. 1990a, ApJ, 360, 279

Poedts, S., Goossens, M., Kerner, W. 1990b, Comp. Phys. Comm., 59, 75

Poedts, S., Kerner, W., Goossens, M. 1989b, J. Plasma Phys., 42, 27

Poedts, S., Tóth, G., Beliën, A. J. C., Goedbloed, J. P. 1996, Solar Physics, submitted

Priest, E. R. 1984, Solar Magnetohydrodynamics, D. Reidel Publishing

Priest, E. R. 1990, in C. T. Russell, E. R. Priest, L. C. Lee (eds.), Physics of magnetic flux ropes, Vol. 58 of *Geophysical Monograph Series*, 1–22, American Geophysical Union

Schnack, D. D., Barnes, D. C., Mikic, Z., Harned, D. S., Caramana, E. J. 1987, J. Comp. Phys., 70, 330

Schwarzschild, M. 1948, ApJ, 107, 1

Zirker, J. B. 1993, Solar Physics, 148, 43

This article was processed by the author using Springer-Verlag LaTeX A&A style file *L-AA* version 3.